PHYSICAL REVIEW C VOLUME 40, NUMBER 5 NOVEMBER 1989

^{24}Mg nuclear moments from ^{24}Mg(200 MeV)+^{208}Pb scattering

D. C. Hensley, E. E. Gross, M. L. Halbert, J. R. Beene, and F. E. Bertrand
Oak Ridge National Laboratory, Oak Ridge, Tennessee 37831

G. Vourvopoulos, D. L. Humphrey, and T. VanCleve
Western Kentucky University, Bowling Green, Kentucky 42101

(Received 27 April 1989)

Differential cross sections for exciting the low-lying states in ^{24}Mg by heavy-ion inelastic scattering were measured with a new technique that uses a 4π γ-ray detector in coincidence with charged-particle detectors. The resulting data were subjected to a coupled-channels analysis to obtain a set of $E2$ and $E4$ matrix elements for exciting the 2_1^+(1.37 MeV), 4_1^+(4.12 MeV), and 2_2^+(4.24 MeV) states of ^{24}Mg as well as the interconnecting and self-coupling matrix elements for these states. Our results disagree with electron scattering measurements for the charge shape of ^{24}Mg. The data on the 2_2^+(4.24 MeV) state is not well accounted for by the asymmetric rotor model.

I. INTRODUCTION

The $E2$ systematics of the lowest 2^+ state of even-even nuclei are well established.[1,2] The same cannot be said for hexadecapole moments, where the existing data are sparse and often contradictory. Where reliable data exist, they have proven valuable in providing nuclear shape information for sensitive testing of nuclear structure models.[3,4] Determination of hexadecapole moments requires absolute measurements of the direct excitation of 4_1^+ states from 0^+ ground states, but data are hard to obtain by heavy-ion scattering because the cross sections are low and because there are severe difficulties, except for the lightest elements, in resolving the 4_1^+ state from neighboring states using conventional particle detection techniques. The method described here overcomes some of these difficulties by use of a nearly 4π γ-ray detector, the spin spectrometer (SS),[5] to obtain the necessary resolution, with high γ-ray efficiency, in coincidence with solid-state particle detectors which provide the information for the differential cross sections. We applied the technique to levels in ^{24}Mg excited by 200 MeV ^{24}Mg ions scattered from a ^{208}Pb target. The beam energy was chosen to provide data in the Coulomb nuclear interference region, where absolute normalization was provided by Rutherford scattering at the forward angles and the interference region provided sensitivity to signs as well as to magnitudes of the matrix elements.

As this is a new technique for obtaining differential cross sections for inelastic scattering, we begin, in Sec. II, with a description of the method as applied to the low-lying states of ^{24}Mg. In Sec. III, we discuss a variety of coupled-channels analyses to extract transitional matrix elements from the data. Finally, in Sec. IV, the results are compared to other measurements and to theoretical calculations.

II. EXPERIMENTAL TECHNIQUE

A beam of 200.05 MeV ^{24}Mg was provided by the Oak Ridge National Laboratory Holyfield Heavy Ion Research Facility tandem accelerator. The target consisted of 400 μg/cm^2 of ^{208}Pb evaporated on the downstream side of a 20 μg/cm^2 carbon foil. The mean beam energy at the center of the ^{208}Pb target was 199.6 ± 0.2 MeV. The inelastically scattered ^{24}Mg ions were detected in position-sensitive solid-state detectors (PSD) in two different experimental arrangements. In one arrangement, a PSD was mounted in a 1.6-m diameter chamber and used to accurately measure the angular distribution of elastically and inelastically scattered ^{24}Mg ions. In the other arrangement, two PSD's covering the entire angular range of interest in the 33-cm diameter scattering chamber of the SS were used to detect scattered ^{24}Mg ions in coincidence with γ rays in the SS. The γ-ray measurements provided the necessary energy resolution, with good efficiency, to resolve the low-lying states of ^{24}Mg. The large scattering chamber measurement provided geometry calibration for the small SS chamber as described later.

Large PSD's 8-mm high by 47- or 27-mm long, were used in order to optimize the acquisition of charged-particle data in the two experimental arrangements. The PSD's were chosen to be relatively thin (500 μ depletion layer) so that beam-velocity light ions would not be stopped in the detectors—only the heavy ions of interest would be stopped. This feature provides a simple, but effective, particle identification scheme which fails only for the neutron pickup reaction. With this one exception, the detectors were able to provide adequate particle identification for the reactions of interest. At the largest angles, where the pickup reaction is a significant contamination, its contribution could be estimated by particle-γ

coincidences to excited states in ^{207}Pb and ^{25}Mg. The PSD's were cooled to about −20 °C to provide a leakage current of under 100 nA at full bias. The position resolution was better than 0.1 mm and the overall energy resolution was 0.7%, not good enough to resolve the first excited state of ^{24}Mg from elastic scattering. A 0.025-mm foil of aluminized Mylar was stretched over the front of the detector to reduce the effect of electrons hitting the detector and to prevent contaminants from collecting on the front surface of the chilled detectors.

In the 1.6-m chamber experiment, a single 47-mm long PSD was mounted 25 cm from the target, where the detector spanned an angular range of about 9°. A 13-wire grid placed over the front of the PSD established angular acceptances. The grid support plate shadowed the edges of the detector to eliminate edge effects. The relative angles of these wires were determined using the precision goniometer of the 1.6-m chamber to rotate the detector while the wires were viewed with a transit. Forward-angle measurements were made on the left-hand and right-hand sides of the beam, which enabled the zero angle relative to the beam direction to be determined to an accuracy of ±0.05°. Charged-particle spectra were then collected at 5° intervals from 10.8° to 55.5° c.m. with a 4° overlap between successive measurements. The grazing angle is about 44° c.m. From these spectra, an angular distribution was constructed for the sum of the elastic plus the first excited state of ^{24}Mg. The absolute normalization was obtained by the requirement that the average ratio to Rutherford scattering of this angular distribution from 10° through 32° c.m. be equal to one. This normalization procedure makes precise knowledge of the geometry, target thickness, and current integrator calibration unnecessary. This initial analysis provided an accurately determined differential cross section for the sum of elastic plus first 2^+ state of ^{24}Mg, which we will refer to as the "raw elastic."

Two PSD's were mounted in the small 33-cm diameter chamber of the SS to cover the entire angular range of interest. A 47-mm long PSD was positioned 12 cm from the target on the right-hand side of the beam and centered at about 40° lab. A 27-mm long PSD was positioned 12.5 cm from the target on the left-hand side of the beam and centered at about 25° lab. There was about a 1.5° angle overlap in the coverage of the two detectors. As in the 1.6-m chamber experiment, the two detectors were cooled and covered with aluminized mylar, but the detectors had no defining collimators for angle definition except for their mounting containers. Essentially all of the active surface of the detectors was visible to the target. Because of limitations on the accuracy of positioning both the target and the detectors in this small chamber, the efficiency and the angles of the setup could only be determined roughly. An angular distribution for the "raw elastic" was accumulated for each PSD. The data from these two pieces of the angular distribution were tied together in the overlap region by the strong angular dependence of the ratio of ^{24}Mg 2^+ (1.37 MeV) yield to "raw elastic" yield, a ratio which was obtained after the γ-coincidence data was analyzed. The resulting SS chamber angular distribution for the "raw elastic" was then compared to the corresponding angular distribution determined from the 1.6-m chamber measurement. Care was taken to insure that the low-energy cutoff was the same for both sets of data. From this comparison it was possible to determine the relation between channel and angle for the SS PSD's and to determine an absolute normalization for each detector.

Before the normalized "raw elastic" could be reduced to a normalized elastic, the contribution from the ^{24}Mg 2^+ state (1.37 MeV) had to be determined. This was accomplished by measuring PSD-γ coincidences with the NaI detectors of the SS. Using this information, the differential cross section for the ^{24}Mg 2^+ state (1.37 MeV) γ ray was generated, Fig. 1, and subtracted from the "raw elastic" to obtain the elastic-scattering differential cross section shown as a ratio to Rutherford scattering in Fig. 2. The uncertainty in the overall normalization is 2%, arising from a 0.1° uncertainty in the angle determination and a 0.2 MeV uncertainty in the beam energy at the center of the target.

The photopeak response of the SS is critical in this analysis. The response is greatly improved by the summing of the pulse heights from clusters of γ-ray detectors. The typical response to a single γ ray involves an average of 1.4 NaI detectors. In order to have the best photopeak efficiency, it is mandatory that the response of any particular detector have added to it the response of its neighbors. The SS has a typical total detection efficiency of about 88% for a single γ ray near 1 MeV, and the cluster summing technique pushes more than 50% of the total response into the photopeak. The absolute γ-ray efficiency of the SS was determined using sources producing two coincident γ rays. A γ ray detected in a Compton-suppressed Ge detector mounted 2 m from the center of the SS triggered a measurement of the response of the SS to the second γ ray. In this way the

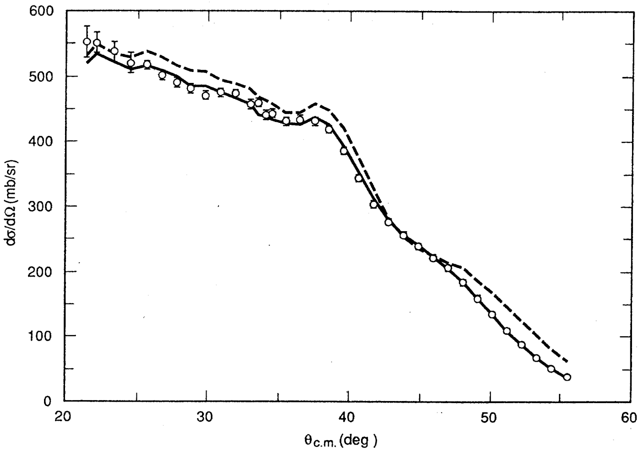

FIG. 1. Measured differential cross section (open circles) for exciting the ^{24}Mg 2_1 state (1.37 MeV) by 200 MeV ^{24}Mg scattering from ^{208}Pb. The solid curve represents our best fit from a $0_1 \leftrightarrow 2_1 \leftrightarrow 4_1 \leftrightarrow 2_2$ symmetric-rotor coupled-channels analysis. The dotted curve shows what happens to this calculation when the static quadrupole moment is set to zero.

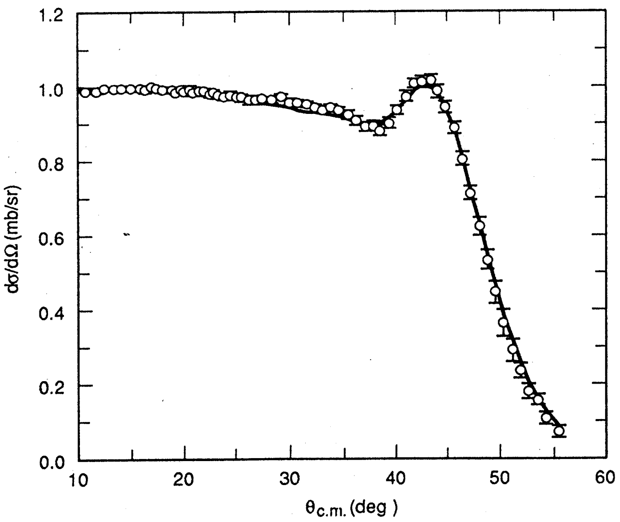

FIG. 2. Measured ^{24}Mg (200 MeV)+^{208}Pb elastic scattering relative to Rutherford scattering (open circles). The solid curve represents our best fit from a $0_1\leftrightarrow 2_1\leftrightarrow 4_1\leftrightarrow 2_2$ symmetric-rotor coupled-channels analysis with either optical potential of Table I.

response of the SS to single γ rays was measured for energies from 120 keV to 2.75 MeV. From the γ ray source calibration, the cluster-summed photopeak efficiency for both gating and peak fitting were determined.

Since the γ rays of interest were emitted by nuclei in flight, it was necessary to correct the observed γ-ray energies for Doppler shifts. This was feasible because the PSD detectors measured both the energy and the angle of the scattered particle, and the angles of all the SS γ-ray detectors were also known. The Doppler energy correction can be as much as 13% for γ rays emitted by scattered ^{24}Mg ions but never more than 1% for γ rays from recoiling ^{208}Pb ions. To identify the origin of the γ rays (i.e., inelastically scattered projectile or recoiling target), each spectrum was Doppler corrected for either the projectile or the recoil. Figure 3 shows the one-cluster γ-ray spectrum for the entire SS in coincidence with PSD events centered near 40° lab. The lower spectrum has been Doppler corrected assuming that the scattered projectile emitted the γ rays, whereas the upper spectrum assumes that the target recoil emitted the γ rays. The sharp peak in the lower spectrum corresponds to the first 2^+ state of ^{24}Mg, and the sharp peaks in the upper spectrum correspond to states in either ^{207}Pb or ^{208}Pb. In most cases, it is immediately obvious from the sharpness of the resulting γ-ray peaks whether the scattered projectile or the target recoil was the source.

A special circumstance arises when γ rays with essentially the same energy are emitted by both the scattered projectile and the recoiling target. The resulting Doppler corrected spectrum will show a sharp peak (the appropriately Doppler-focused peak) on a broad peak (the defocused peak). Depending on the relative yields of the two peaks, this focusing may be sufficient to permit the yield of the sharp peak to be extracted, but this is rarely satisfactory. On the other hand, since the projectile and the recoil go in different directions, and with very different velocities, the Doppler shifts associated with a given NaI detector may differ enough so that the resulting lab energies of the two γ rays can be resolved. To illustrate this point, we show in Fig. 4 the spectrum from the entire SS gated by the ^{24}Mg 2^+ (1.37 MeV) γ ray and in coincidence with the PSD centered at 40° lab. Figure 4(a) shows the spectrum Doppler corrected for projectile emission and it clearly indicates a strong contribution from the ^{24}Mg 4^+ state (4.12 MeV), which decays to the first 2^+ state by emission of a 2.75-MeV γ ray. Figure 4(b) shows the same spectrum but Doppler corrected for target recoil emission and indicates a substantial interference with the decay from the ^{208}Pb 3^- state (2.61 MeV),

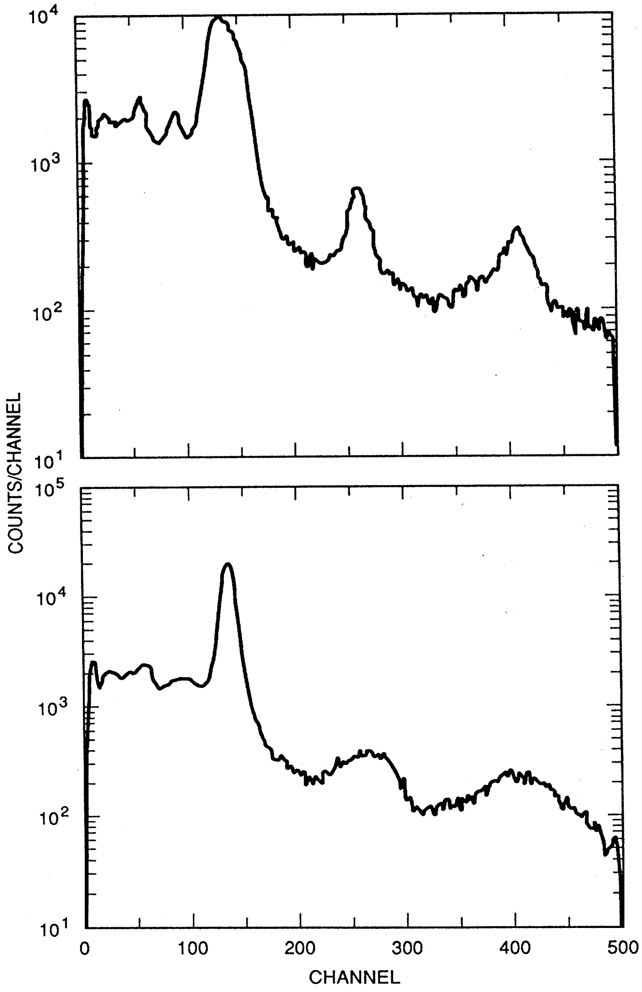

FIG. 3. Single-cluster γ-ray spectra from ^{24}Mg (200 MeV)+^{208}Pb inelastic scattering. The upper spectrum has been Doppler shifted for target recoil emission. Sharp peaks at channels 57 and 90 are associated with the first two excited states in ^{207}Pb. Focused peaks at channels 261 and 409 are associated with two excited states in ^{208}Pb. The lower spectrum has been Doppler corrected for emission from an inelastically scattered projectile, and shows a sharp peak in channel 137, which we associate with the ^{24}Mg 2^+ state at 1.37 MeV.

which was mutually excited with the first 2^+ state of ^{24}Mg. Figure 4(c) shows the same data as in Fig. 4(a) but for only a 30% subset of NaI detectors centered along the inelastically scattered ^{24}Mg direction, so chosen as to maximize the Doppler separation of ^{24}Mg and ^{208}Pb γ rays. The relationship of the coincidence yield of γ rays detected in the subset of the SS to the differential scattering cross section depends on the γ-ray angular correlation. This effect was corrected for in an iterative procedure. The first step was to assume that the γ rays were emitted isotropically in the rest frame of the emitter. This provided an initial differential cross section for the ^{24}Mg 4_1^+ state (4.12 MeV). The same method was used to separate the ^{24}Mg 2_2^+ state (4.24 MeV) γ ray from the ^{208}Pb 2^+ state (4.208 MeV) γ ray to obtain an initial differential cross section for this state. After the coupled-channels fit to this initial data set was obtained, as described in Sec. III, the predicted γ-ray angular correlations for the 4_1^+ and 2_2^+ states were used to correct the effective efficiency for γ-ray detection. The calculated efficiencies include the effect of attenuation of the nuclear alignment due to the hyperfine interaction.[6] The predicted γ-ray efficiencies of the used 30% portion of the SS relative to its geometric efficiency is shown in Fig. 5(a) for the 4_1^+ state (solid curve) and the 2_2^+ state (dashed curve). The initial 4_1^+ and 2_2^+ state data were then corrected for the calculated angular correlations of Fig. 5(a) and the coupled-channels fitting was repeated for the

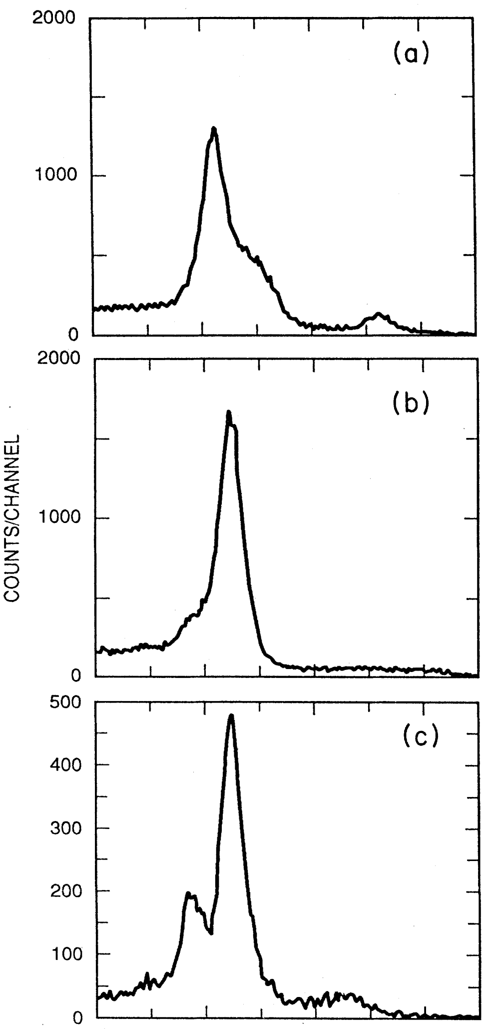

FIG. 4. Single-cluster γ-ray spectra projected from two-cluster events where the other cluster fell within a gate set on the 1.37 MeV γ ray. (a) Spectra from the entire SS but Doppler corrected as if emitted from the recoiling target. (b) The same spectra Doppler corrected as if the γ rays were emitted from the scattered projectile. (c) Projectile-focused spectra obtained by using a 30% subset of the SS data chosen so as to maximize the separation of ^{24}Mg ($4_1 \leftrightarrow 2_1$ 2.75 MeV) and ^{208}Pb ($3^1 \leftrightarrow 0_1^+$ 2.61 MeV) γ rays.

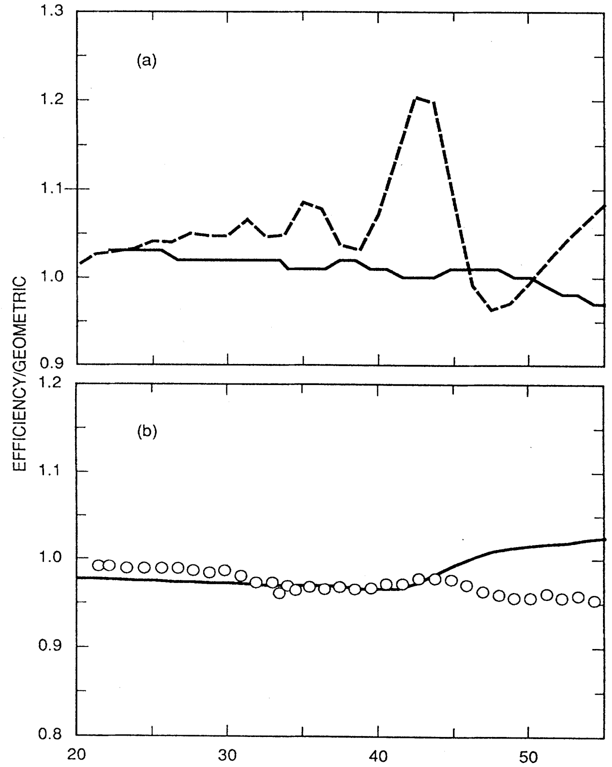

FIG. 5. The curves are predicted γ-ray efficiencies relative to geometric (isotropic) efficiency for a 30% subsection of the SS detectors which is chosen to be centered about the ^{24}Mg scattered direction. The x axis is the scattered ^{24}Mg direction. The predictions result from the coupled-channels fits to the differential cross sections. The solid curve in (a) is for the $4_1 \leftrightarrow 2_1$ (2.75 MeV) transition and the dashed curve is for the $2_2 \leftrightarrow 2_1$ (2.87 MeV) transition. The solid curve in (b) is for the $2_1 \leftrightarrow 0_1$ (1.37 MeV) transition compared to the data (circles) derived from all detectors in the SS.

corrected data set. The new γ-ray correlations were found to be essentially unchanged from the previous ones. The procedure thus converged in one iteration. This procedure was checked with the data from 2_1^+ state where all the SS detectors were used. Figure 5(b) compares the calculated γ-ray efficiency of the 30% subset of the SS centered along the inelastically scattered ^{24}Mg direction with the measured efficiency for the 2_1^+ state. Agreement between calculation and experiment is excellent, except for the largest angles where there is an apparent 7% discrepancy. The final 4_1^+ and 2_2^+ data are shown in Figs. 6 and 7.

III. ANALYSIS

A. Introduction

The analysis of our ^{24}Mg data was done using the computer program ECIS (Ref. 7) to perform symmetric-rotor coupled-channels[8] calculations with nonrelativistic kinematics. Most of the calculations employed 650 partial waves and a matching radius of 55 fm. The final calculations required a minimum of 750 partial waves and a matching radius of 65 fm before results were found to be independent of these parameters. A few calculations applying the asymmetric-rotor model[9] to ^{24}Mg were also done. The states and couplings included in the analysis are shown in Fig. 8. As we will only be dealing with even-parity states, we will omit the "+" superscript on the level identification for the remainder of this paper. A calculation including the 6_1 state (8.11 MeV) was also performed to assess the effect of including this state. The coupled-channels analysis of a level scheme like that shown in Fig. 8, applied to a data set such as that shown in Figs. 1, 2, 6, and 7, involves hundreds of lengthy calculations before the "final" calculation is obtained. The procedure we have followed has evolved over several years, and has been described in detail in previous publications.[10–13]

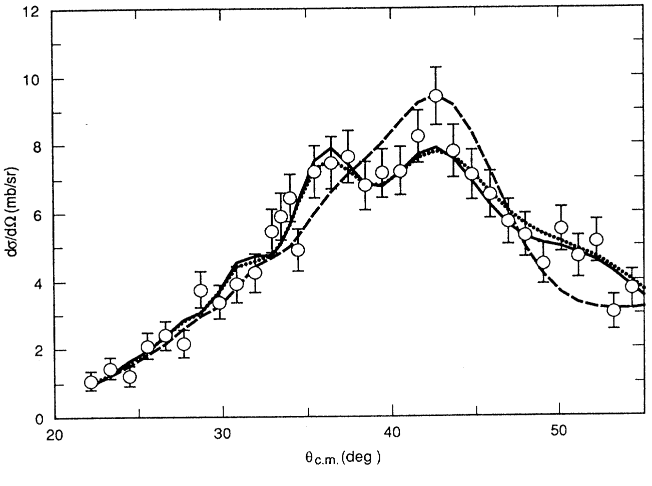

FIG. 6. Measured differential cross section (open circles) for exciting the ^{24}Mg 4_1 state (4.12 MeV) by 200 MeV ^{24}Mg scattering from ^{208}Pb. The solid curve represents our best fit from a $0_1 \leftrightarrow 2_1 \leftrightarrow 4_1 \leftrightarrow 2_2$ symmetric-rotor coupled-channels analysis. The dotted curve shows the effect on the 4_1 state of including the 6_1 state (8.11 MeV) in the calculation. The dashed curve shows the effect of decreasing the $M(E4;0_1 \leftrightarrow 4_1)$ matrix element from the best-fit value (solid curve) of 142 $e$fm^4 to the electron scattering value (Refs. 24 and 25) of 41 $e$fm^4.

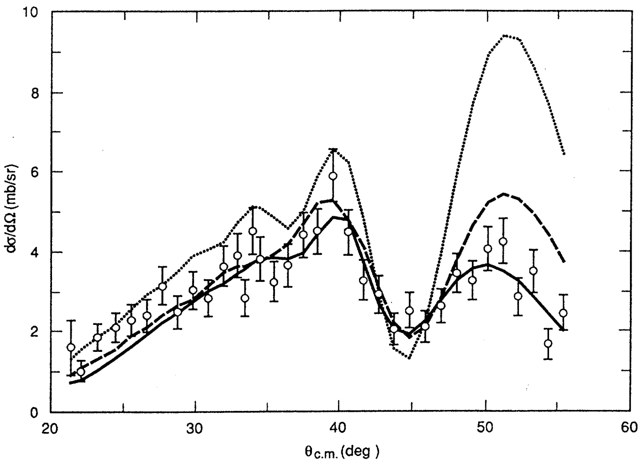

FIG. 7. Measured differential cross section (open circles) for exciting the ^{24}Mg 2_2 state (4.24 MeV) by 200 MeV ^{24}Mg scattering from ^{208}Pb. The solid curve represents our best fit from a $0_1 \leftrightarrow 2_1 \leftrightarrow 4_1 \leftrightarrow 2_2$ symmetric-rotor coupled-channels analysis. The dashed curve represents the minimum χ^2 fit by varying the parameter γ_c ($=8.5°$) of the asymmetric-rotor model. The dotted curve illustrates the effect of using γ-decay values (Ref. 28) for the $M(E2;0 \leftrightarrow 2_2)$ and $M(E2;2_1 \leftrightarrow 2_2)$ matrix elements and relative signs predicted by the shell model (Ref. 32).

B. Optical potential

The Coulomb potential generated by the deformed ^{24}Mg was taken to be due to a uniform charge density, ρ_0,

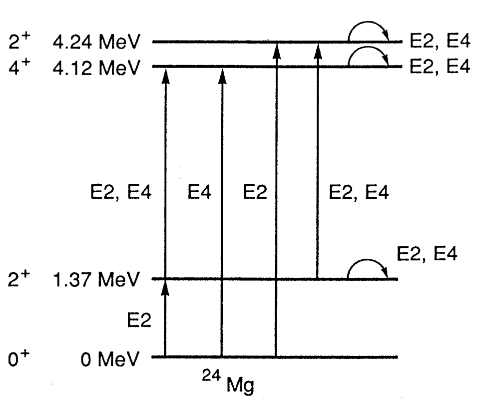

FIG. 8. Levels and transitions in ^{24}Mg explicitly accounted for in the present coupled-channels analysis.

out to a deformed radius, $R_c(\theta)$:

$$\rho(r,\theta)=\begin{cases}\rho_0, & r\le R_c(\theta)\\ 0, & r>R_c(\theta)\end{cases} \tag{1}$$

$$R_c(\theta)=1.2\times(24)^{1/3}[1+\beta_2^cY_{20}(\theta)+\beta_4^cY_{40}(\theta)]\ \text{fm}\ , \tag{2}$$

and the net charge was normalized to $12e$. The Coulomb potential generated by ^{208}Pb was taken as that from a point with charge $82e$. The nuclear optical potential was taken to have the usual Woods-Saxon form with a radius given by

$$R_n(\theta)=r_n\times[(24)^{1/3}+(208)^{1/3}]\\ \times[1+\beta_2^nY_{20}(\theta)+\beta_4^nY_{40}(\theta)+\cdots]\ \text{fm}\ , \tag{3}$$

where the r_n can have different values for the real and imaginary (volume) potentials. An essential feature was the constraint on nuclear deformation parameters, β_L^n, imposed by the Hendrie scaling procedure.[14] The geometrical operation of rolling the spherical "projectile" (^{208}Pb) over the deformed "target" surface [^{24}Mg charge distribution given by Eq. (2)] will trace out a surface described by Eq. (3). The β_L^n were determined from a multipole expansion[11] of this surface and we ignored terms for $L\ge 6$, since the $L=6$ terms were found to give negligible contributions. In this analysis, therefore, the nuclear deformation parameters were not independent parameters but were tied to the charge deformations by the procedure just described.

The parameters to be fitted were the Woods-Saxon potential parameters V, r_V, a_V, W, r_W, a_W, and the matrix elements indicated in Fig. 8. As starting values for the optical potential we used values previously found[12] for ^{20}Ne (131 MeV)+^{208}Pb. The matrix element for exciting the first 2^+ state in the symmetric rotor model is given by

$$M(E2;0\leftrightarrow 2_1)=\int\rho(r,\theta)r^2Y_{20}(\theta)d\tau\ . \tag{4}$$

As a starting value for this matrix element we used the "adopted" value[1] of $(-20.8\pm0.3)\ e\text{fm}^2$, where we use the sign convention employed in the coupled-channels program ECIS.[7] The value of β_2^c that generates 20.8 $e$fm^2 from Eqs. (1), (2), and (4) (with $\beta_4^c=0$, initially) is $\beta_2^c=+0.504$. The value of $M(E2;0\leftrightarrow 2_1)$ that best fits the 2_1 differential cross section (solid curve in Fig. 1) over the entire angular range is

$$M(E2;0_1\leftrightarrow 2_1)=(-20.44\pm0.27)\ e\text{fm}^2\ , \tag{5}$$

which is in excellent agreement with the adopted value.[1] The error includes contributions from statistics on the fit ($\pm$0.09 $e$fm^2), uncertainty in the beam energy at the center of the target ($\pm$0.03 $e$fm^2), uncertainty in the angle calibration ($\pm$0.09 $e$fm^2), uncertainty due to correlations with other matrix elements ($\pm$0.15 $e$fm^2), and uncertainty in the overall normalization ($\pm$0.18 $e$fm^2), as described in the experimental section. Actually, the value quoted for this matrix element, and the matrix elements to follow, resulted from a final adjustment of *all* matrix elements in a full $0_1\leftrightarrow 2_1\leftrightarrow 4_1\leftrightarrow 2_2$ calculation, but we present here a time sequence of how the analysis proceeded. This result, Eq. (5), is dominated by Coulomb excitation effects and is therefore insensitive to the details of the optical potential or the amount of β_4^c deformation as long as β_2^c is adjusted, along with β_4^c, as required in Eq. (4). The quality of fit that this value provides for the 2_1 differential cross section can be judged from the solid curve in Fig. 1. Except for the first four data points, the errors shown on the measured differential cross sections have been uniformly adjusted from the statistical errors such that the minimum χ^2 equaled the number of data points being fitted. The first four data points have an additional uncertainty due to an observed nonlinear behavior in the PSD.

With $M(E2;0_2\leftrightarrow 2_1)$ fixed at -20.44 $e$fm^2, with values of $M(E2;0_1\leftrightarrow 2_2)$, $M(E2;2_1\leftrightarrow 2_2)$, and $M(E4;2_1\leftrightarrow 2_2)$, that roughly account for the magnitude and shape of the 2_2 cross section, and with symmetric-rotor values for all other matrix elements in Fig. 8, we searched on the optical parameters for a fit to the elastic scattering data. Heavy-ion scattering near the Coulomb barrier is primarily a nuclear surface phenomenon. This leads to an ambiguity in the optical potential and we therefore show two potentials that produce equally good fits to the elastic scattering (Fig. 2). The two potentials are compared in Fig. 9 for the real potential and in Fig. 10 for the imaginary potential, and are tabulated in Table I. They differ primarily in the depth and radius of the real and imaginary potentials but they have the same value near the strong absorption radius. Both potentials yield identical values for the matrix elements.

C. $0\leftrightarrow 2_1\leftrightarrow 4_1$ calculations

With the optical potential established as one of the sets in Table I, and symmetric-rotor values for the $2_1\leftrightarrow 4_1$ matrix elements, a series of $0\leftrightarrow 2_1\leftrightarrow 4_1$ calculations were made at discrete values of $M(E2;0_1\leftrightarrow 2_1)$, while search-

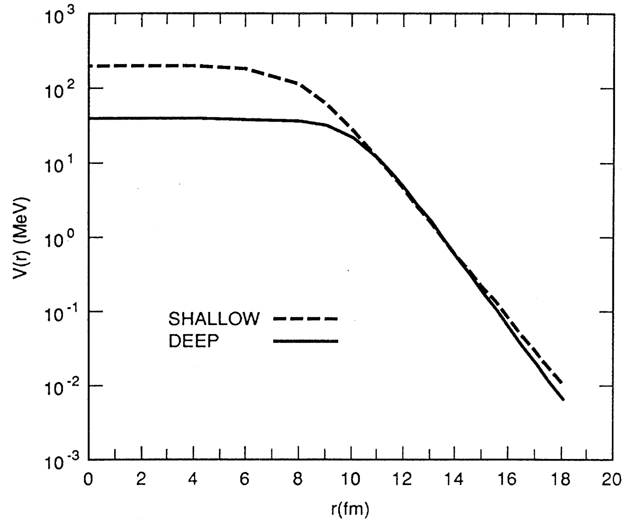

FIG. 9. The real part of the optical potential for the reaction ^{24}Mg (200 MeV)+^{208}Pb vs radial distance. Two Woods-Saxon potentials from Table I are shown which provide equally good fits to the elastic scattering and which yield essentially the same values for the transition matrix elements.

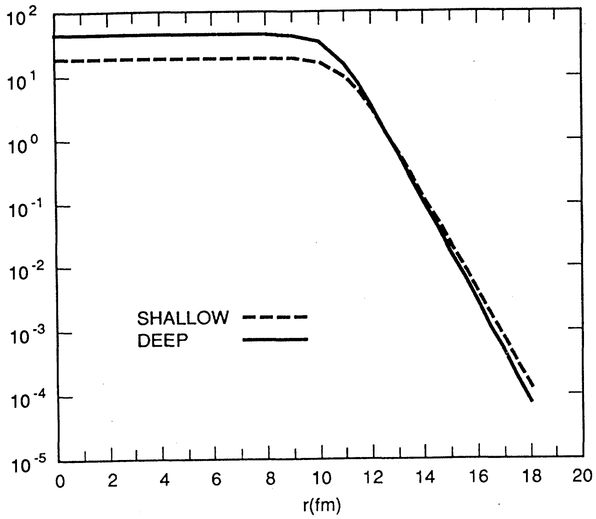

FIG. 10. Imaginary part of the optical potential for the reaction ^{24}Mg (200 MeV)+^{208}Pb vs radial distance for the two Woods-Saxon potentials in Table I.

ing on $M(E2;2_1\leftrightarrow2_1)$ and $M(E4;2_1\leftrightarrow2_1)$ at each step to obtain a fit to the 2_1 cross section. In this way the $M(E2;0_1\leftrightarrow2_1)$ value quoted above [Eq. (5)] was obtained as well as the following values for the 2_1 state reorientation matrix elements:

$$M(E2;2_1\leftrightarrow2_1)=(+27\pm5)\ e\text{fm}^2 \tag{6}$$

and

$$M(E4;2_1\leftrightarrow2_1)=(+1110\pm240)\ e\text{fm}^4\ . \tag{7}$$

To illustrate the importance of correlations between the matrix elements in an extreme way, we show in Fig. 1, as a dotted curve, the effect on the calculated 2_1 cross section if the reorientation matrix element $M(E2;2_1\leftrightarrow2_1)$ is set to zero. The $E2$ reorientation matrix element [Eq. (6)] implies a spectroscopic quadrupole moment of

$$Q_{2_1}=(-20\pm4)\ e\text{fm}^2\ , \tag{8}$$

which is close to the rotational-model expectation of $-18.5\ e\text{fm}^2$.

To fit the 4_1 cross section, a series of calculations were made for a range of β_2^c and β_4^c values which generated $M(E2;0_1\leftrightarrow2_1)=-20.44\ e\text{fm}^2$, while searching on $M(E2;2_1\leftrightarrow4_1)$, $M(E4;2_1\leftrightarrow4_1)$, $M(E2;4_1\leftrightarrow4_1)$, and $M(E4;4_1\leftrightarrow4_1)$ at each step. In each calculation the nuclear deformations were fixed at their scaled values as described above. The minimum χ^2 fit to the 4_1 data (solid curve in Fig. 6) was obtained with $\beta_2^c=+0.469$ and $\beta_4^c=+0.065$ or a value of $M(E4;0_1\leftrightarrow4_1)$ given by

$$\begin{aligned}M(E4;0_1\leftrightarrow4_1)&=\int\rho(r,\theta)r^4Y_{40}(\theta)d\tau\\&=(+142\pm9)\ e\text{fm}^4\ ,\end{aligned} \tag{9}$$

where the error includes a contribution from the uncertainty on the $M(E2;0_1\leftrightarrow2_1)$ matrix element and correlations with the other matrix elements.

In addition, the following matrix element values resulted from the procedure just outlined:

$$M(E2;2_1\leftrightarrow4_1)=(-32\pm6)\ e\text{fm}^2\ , \tag{10}$$

$$M(E4;2_1\leftrightarrow4_1)=(-565\pm210)\ e\text{fm}^4\ , \tag{11}$$

$$M(E2;4_1\leftrightarrow4_1)=(+28\pm130)\ e\text{fm}^2\ , \tag{12}$$

$$M(E4;4_1\leftrightarrow4_1)=(+2400\pm1050)\ e\text{fm}^4\ . \tag{13}$$

A few $0\leftrightarrow2_1\leftrightarrow4_1\leftrightarrow6_1$ rotational-model calculations were investigated including the 6_1 state at 8.11 MeV to assess the effect of this state on the aforementioned results. The effect of including this state with rotational-model matrix elements but no direct excitation from the ground state is essentially negligible on the 2_1 state. The effect of including the 6_1 state on the 4_1 state is also small as can be seen by the dotted curve in Fig. 6.

D. $0\leftrightarrow2_1\leftrightarrow2_2$ symmetric-rotor calculations

Matrix elements involving the 2_2 state (4.24 MeV) were determined initially with $0_1\leftrightarrow2_1\leftrightarrow2_2$ couplings and using symmetric-rotor model form factors but the final values reported later come from a full $0_1\leftrightarrow2_1\leftrightarrow4_1\leftrightarrow2_2$ calculation. Again allowing χ^2 to determine the best-fit values and uncertainties we obtain

$$M(E2;0_1\leftrightarrow2_2)=(+4.5\pm2.0)\ e\text{fm}^2\ , \tag{14}$$

$$M(E2;2_1\leftrightarrow2_2)=(-11\pm9)\ e\text{fm}^2\ , \tag{15}$$

$$M(E4;2_1\leftrightarrow2_2)=(+230\pm150)\ e\text{fm}^4\ , \tag{16}$$

$$M(E2;2_2\leftrightarrow2_2)=(-22\pm350)\ e\text{fm}^2\ , \tag{17}$$

$$M(E4;2_2\leftrightarrow2_2)=(+870\pm3500)\ e\text{fm}^4\ . \tag{18}$$

TABLE I. Woods-Saxon optical-model parameters obtained in the full $0_1\leftrightarrow2_1\leftrightarrow4_1\leftrightarrow2_2$ coupled-channels fit to the data (see text). V is the real nuclear potential and W is the imaginary nuclear potential (volume).

	V (MeV)	r_V (fm)	a_V (fm)	W (MeV)	r_W (fm)	a_W (fm)
Shallow potential	32.03	1.156	0.946	26.0	1.244	0.534
Deep potential	229.0	0.933	0.956	70.3	1.204	0.507

The best fit to the 2_2 data using symmetric-rotor model form factors is shown as the solid curve in Fig. 7.

In Coulomb excitation determinations of Q_2 for the first 2^+ state by the reorientation effect, there is usually an ambiguity in the value of Q_{2_1} due to the influence of the 2_2 state. This influence can either be constructive or destructive depending on the relative sign of the product of the following four matrix elements:

$$p_4 = M(E2;0_1 \leftrightarrow 2_1),\ M(E2;0_1 \leftrightarrow 2_2),\ M(E2;2_1 \leftrightarrow 2_2),\ M(E2;2_1 \leftrightarrow 2_1)\ . \tag{19}$$

Although this ambiguity is a small effect in the case of ^{24}Mg, we can report, from the signs of the appropriate matrix elements determined here, that $p_4 > 0$. In any case, the effect of the second 2^+ state on our result [Eq. (8)] is already accounted for, as this state is explicitly included in the coupled-channels analysis.

Another 2^+ state that could influence Q_2 is the giant quadrupole resonance (GQR). Although the GQR is highly fragmented in ^{24}Mg,[15] we estimated its effect by placing a 2^+ state at the expected center of gravity for the GQR, 63 $A^{-1/3} = 21.8$ MeV, containing 60% of the energy-weighted sum rule.[15] Depending on the assumed sign and magnitude for the $M(E2;2_1 \leftrightarrow 2_{\mathrm{GQR}})$ matrix element, we find that inclusion of such a state can increase the extracted Q_2 value by 2–4 %. Coupling to the GQR is seen to be more important in affecting the value of Q_2 than coupling to the giant dipole resonance (GDR), where Fewell[16] has estimated the effect to be a reduction in Q_2 by 0.5%.

E. $0_1 \leftrightarrow 2_1 \leftrightarrow 4_1 \leftrightarrow 2_2$ asymmetric-rotor calculations

The earlier analysis using symmetric-rotor model form factors provides a satisfactory account of our inelastic scattering data. However, a natural way to account for the second 2^+ state is by postulating a triaxial shape for ^{24}Mg. A few asymmetric-rotor model analyses,[17,18] have been applied to previous ^{24}Mg data and several theoretical calculations[19–21] have predicted triaxial shapes for this nucleus. We therefore subjected our data to an asymmetric-rotor model analysis using the generalization of the Davydov-Filippov model[8] due to Baker,[22] who included hexadecapole deformation and a method for calculating the proper scaling for the nuclear β and γ parameters of the model. The best asymmetric-rotor fit to the 2_2 state is shown as the long-dashed curve in Fig. 7, and is for a value $\gamma_c = 8.5°$, far from the expected value of 22° (on the basis of energy-level spacings[23]) and with a χ^2 value five times larger than the fit based on symmetric-rotor model form factors (solid curve in Fig. 7). Although this asymmetric-rotor calculation gives a reasonable account for the 4_1 state, the fit to the 2_1 state has a χ^2 value three times larger than that using symmetric-rotor form factors. Relaxing the Hendrie scaling procedure[13] for determining the nuclear deformation parameters was also investigated. The asymmetric-rotor model fit to the 2_1 state could be considerably improved by reducing the nuclear β_2 parameters by 20% and the nuclear β_4 parameters by about 40% from their Hendrie scaled values. A further failure of the asymmetric-rotor model for ^{24}Mg is the prediction that the product of the three matrix elements $M(E2;0_1 \leftrightarrow 2_1)$, $M(E2;0_1 \leftrightarrow 2_2)$, and $M(E2;2_1 \leftrightarrow 2_2)$ is less than zero, in the sign convention used in ECIS,[7] whereas the above fit to the data utilizing symmetric-rotor model form factors appear to require this product to be positive. We conclude that the asymmetric-rotor model is not capable of representing the matrix elements needed to fit this set of data.

IV. COMPARISON TO OTHER DATA AND TO THEORY

The literature on Coulomb excitation of the ^{24}Mg 2_1 state (1.37 MeV) is rather extensive.[1] The same cannot be

TABLE II. Comparison of various measurements and theoretical predictions for $M(E2;0_1 \leftrightarrow 2_1)$ and $M(E4;0_1 \leftrightarrow 4_1)$ matrix elements and for corresponding β_2 and β_4 Coulomb deformation parameters for $r_c = 1.2$ fm.

Reaction or theory	$M(E2;0_1 \leftrightarrow 2_1)$ ($e$fm^2)	$M(E4;0_1 \leftrightarrow 4_1)$ ($e$fm^4)	Reference	β_2	β_4
^{24}Mg+^{208}Pb, 200 MeV	-20.4 ± 0.3	$+142\pm9$	Present	$+0.469$	$+0.065$
e,e' 183 and 250 MeV	-21.8 ± 1.0	$+41\pm13$	24	$+0.569$	-0.105
e,e' 218 MeV	-21.3 ± 0.8	$+45\pm3$	25	$+0.555$	-0.094
p,p' 800 MeV	-18.7 ± 0.8	$+70\pm17$	29	$+0.469$	-0.020
α,α' 104 MeV	-19.3 ± 0.7[a]	$+74\pm17$[a]	30	$+0.481$	-0.020
Various Coulomb excitations	-20.8 ± 0.3		1		
Hartree-Fock	-20.33	$+117$	31	$+0.482$	$+0.029$
Potential energy surface	-20.2	$+84$	20	$+0.500$	-0.019
Shell model	19.7	$+40.5$	32	$+0.557$	-0.100
Triaxial-rotor model	-16.4		19		

[a] Calculated using Eqs. (4) and (6) with the reported (Ref. 30) nuclear deformations and the imaginary optical potential radius.

said for excitation of the 4_1 state (4.12 MeV). We choose to compare our results primarily with measurements which report values and uncertainties for both $M(E2;0_1\leftrightarrow 2_1)$ and $M(E4;0_1\leftrightarrow 4_1)$. These are summarized in Table II along with a variety of theoretical predictions. Also shown in Table II are β_2^c and β_4^c values corresponding to these matrix elements obtained by satisfying Eqs. (4) and (6) simultaneously with the charge density of Eq. (1) and the radius of Eq. (2). There is reasonable agreement on the value of $M(E2;0_1\leftrightarrow 2_1)$, but a wide variation in both experimental and theoretical values for $M(E4;0_1\leftrightarrow 4_1)$ and the corresponding β_4^c is evident. The charge distribution implied by the electron scattering measurements[24,25] is compared to the present measurement in Fig. 11. The electron results find a sizable negative hexadecapole charge deformation ($\beta_4^c=-0.1$), whereas the present measurement is consistent with a small positive hexadecapole charge deformation ($\beta_4^c=+0.065$). Sensitivity to the $M(E4;0_1\leftrightarrow 4_1)$ matrix element is illustrated in Fig. 6, which shows the fitted angular distribution for an $M(E4;0_1\leftrightarrow 4_1)$ value of 41 $e\text{fm}^4$ (dashed curve), which is the electrons scattering result,[24] compared to 142 $e\text{fm}^4$ (solid curve), which is the best-fit value to our data. Our result for $M(E4;0_1\leftrightarrow 4_1)$, although dominated by Coulomb excitation, is influenced by nuclear excitation and therefore depends on the nuclear deformation scaling employed in our analysis.

A summary of a variety of measurements and calculations for the spectroscopic quadrupole moment of the ^{24}Mg 2_1 state (1.37 MeV) is shown in Table III. The present measurement suggests that the first 2^+ state of ^{24}Mg has a spectroscopic quadrupole moment close to the rotational value, which agrees with theoretical predictions and with the measurements of Fewell *et al.*[26] Again, it should be pointed out that our result for the quadrupole moment is strongly affected by the nuclear matter distribution, whereas the other experiments are purported to be Coulomb reorientation measurements and therefore supposedly uncontaminated by nuclear effects. However, in a prior study of 70 MeV ^{12}C inelastic scattering from the even Nd isotopes,[27] it had been shown that the method used here yielded spectroscopic quadrupole moments consistent with Coulomb reorientation measurements.

TABLE III. Comparison of various measurements and theoretical predictions for the static quadrupole moment of ^{24}Mg.

Reaction or theory	Q_{2_1} ($e$fm^2)	Reference
^{24}Mg+^{208}Pb, 200 MeV	-20 ± 4	Present
^{35}Cl+^{24}Mg	-38 ± 16	33
^{35}Cl+^{24}Mg	-24.3 ± 3.5	34
^{16}O+^{24}Mg	-30.5 ± 6.4	35
^{32}S+^{24}Mg	-24 ± 6	36
^{24}Mg+Pt, Au	-27 ± 5	37
^{24}Mg+^{208}Pb, 90 MeV	-17.8 ± 1.3	38
Shell model	-19.8	32
Hartree-Fock	-17.8	39
Hartree-Fock	-19.7	31
Triaxial rotor	-15	19
Rotational model	-18.5	Present

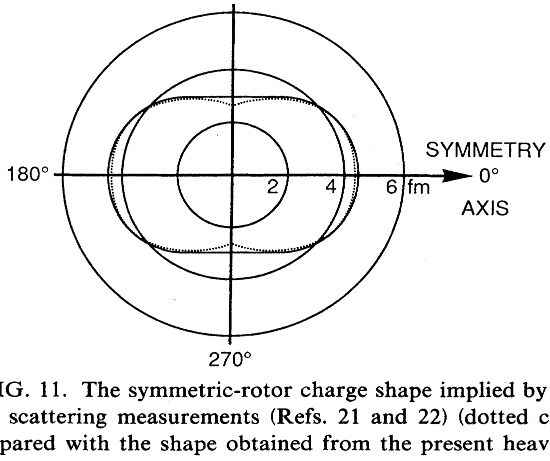

FIG. 11. The symmetric-rotor charge shape implied by electron scattering measurements (Refs. 21 and 22) (dotted curve) compared with the shape obtained from the present heavy-ion scattering experiment and analysis (solid curve).

Table IV contains a summary of experimental and theoretical results for matrix elements involving the 2_2 state (4.24 MeV). The values for signs of the matrix elements $M(E2;0_1\leftrightarrow 2_2)$ and $M(E2;2_1\leftrightarrow 2_2)$, are well determined by fitting the shape and magnitude of the 2_2 state. We agree, within the errors, with γ decay and branching ratio measurements[28] on the values of these matrix elements. The dotted curve in Fig. 7 shows the effect of changing these two matrix elements from our best-fit values to the γ-decay values, while keeping the signs as determined here.

In summary: Use of a nearly 4π γ-ray detector (the spin spectrometer) in coincidence with solid-state particle detectors has provided the means of obtaining a set of internormalized 0_1, 2_1, 4_1, and 2_2 differential cross-section data for ^{24}Mg. Performing the experiment in the Coulomb nuclear interference region allowed an absolute normalization for this data set to Rutherford scattering at forward angles, whereas the structure in the interference region provided a sensitivity to signs as well as magnitudes of the matrix elements. Subjecting the data set to

TABLE IV. Comparison of various measurements and theoretical predictions of transitional matrix elements involving the second 2^+ state (4.24 MeV) of ^{24}Mg.

Reaction or theory	$M(E2;0_1\leftrightarrow 2_2)$ ($e$fm^2)	$M(E2;2_1\leftrightarrow 2_2)$ ($e$fm^2)	Reference
^{24}Mg+^{208}Pb, 200 MeV	$+4.5\pm2.0$	-11 ± 9	Present
γ decay	5.4 ± 0.3^a	7.0 ± 0.4^a	26
e,e' 218 MeV	5.2 ± 0.3		24
Hartree-Fock	5.3	13.3	31
Shell model	$+6.5$	$+8.7$	32
Triaxial rotor	3.9	5	19

[a] Average from γ-ray lifetime and branching ratio measurements.

a rotational-model coupled-channels analysis then produced excellent fits to the differential cross sections and a set of interdependent matrix elements subject to the restriction that nuclear deformations were tied to Coulomb deformations by a Hendrie scaling procedure.[14] We find a prolate charge distribution with a small positive hexadecapole moment in disagreement with results deduced from inelastic electron scattering,[24,25] which imply a prolate shape with a sizable negative hexadecapole moment. We also find a spectroscopic quadrupole moment for the first 2^+ state that is near the rotational model value, in agreement with the latest measurement[26] and with theoretical predictions. Finally, we find that the asymmetric-rotor model offers a poor description of this data set.

ACKNOWLEDGMENTS

We are indebted to F. Todd Baker for advice and help on the calculations, particularly the asymmetric-rotor model calculations. We have had several helpful conversations with F. K. McGowan and I. Y. Lee concerning rotational-model matrix elements. We are also grateful to J. B. McGrory for the shell-model results. The research at Western Kentucky University was supported by the National Science Foundation under Grant No. PHY-8519914. The research at Oak Ridge National Laboratory was supported by the U.S. Department of Energy under Contract No. DE-AC05-84OR21400 with Martin Marietta Energy Systems, Inc.

---

[1] S. Raman, C. H. Malarkey, W. T. Milner, C. W. Nestor, and P. H. Stelson, At. Nucl. Data Tables **36**, 1 (1987).

[2] S. Raman, C. W. Nestor, and K. H. Bhatt, Phys. Rev. C **37**, 797 (1988).

[3] E. Eichler, N. R. Johnson, R. O. Sayer, D. C. Hensley, and L. L. Riedinger, Phys. Rev. Lett. **30**, 568 (1973).

[4] F. Todd Baker, Alan Scott, T. P. Cleary, J. L. C. Ford, E. E. Gross, and D. C. Hensley, Nucl. Phys. **A321**, 222 (1979).

[5] M. Jääskeläinen, D. G. Sarantites, R. Woodward, F. A. Dilmanian, J. T. Hood, R. Jaaskelainen, D. C. Hensley, M. L. Halbert, and J. H. Barker, Nucl. Instrum. Methods **204**, 385 (1983).

[6] R. E. Horstman, J. L. Eberhardt, H. A. Doubt, C. M. E. Otten, and G. Van Middelkoop, Nucl. Phys. **A248**, 291 (1975).

[7] J. Raynal, Phys. Rev. C **23**, 2571 (1981).

[8] T. Tamura, Rev. Mod. Phys. **37**, 679 (1965).

[9] A. S. Davydov and G. F. Filippov, Nucl. Phys. **8**, 237 (1958).

[10] D. L. Hillis, E. E. Gross, D. C. Hensley, C. R. Bingham, F. T. Baker, and A. Scott, Phys. Rev. C **16**, 1467 (1977).

[11] F. T. Baker, A. Scott, E. E. Gross, D. C. Hensley, and D. L. Hillis, Nucl. Phys. **A284**, 135 (1977).

[12] E. E. Gross, T. P. Cleary, J. L. C. Ford, D. C. Hensley, and K. S. Toth, Phys. Rev. C **17**, 1665 (1978).

[13] F. T. Baker, A. Scott, E. E. Gross, D. C. Hensley, and D. L. Hillis, Nucl. Phys. **A325**, 525 (1979).

[14] D. L. Hendrie, Phys. Rev. Lett. **31**, 478 (1973).

[15] F. E. Bertrand, K. van der Borg, A. G. Drentje, M. N. Harakeh, J. van der Plicht, and A. van der Woude, Phys. Rev. Lett. **40**, 635 (1978).

[16] M. P. Fewell, Ph.D. thesis, Australian National University, 1978 (unpublished).

[17] K. van der Borg, M. N. Harakeh, and B. S. Nilsson, Nucl. Phys. **A125**, 31 (1979).

[18] J. Nurzynski, C. H. Atwood, T. R. Ophel, D. F. Hebbard, B. A. Robson, and R. Smith, Nucl. Phys. **A399**, 259 (1983).

[19] D. Kurath, Phys. Rev. C **5**, 768 (1972).

[20] G. Leander and S. E. Larsson, Nucl. Phys. **A239**, 93 (1975).

[21] B. Grammaticos, Nucl. Phys. **A252**, 90 (1975).

[22] F. T. Baker, Nucl. Phys. **A331**, 39 (1979).

[23] S. W. Robinson and R. D. Bent, Phys. Rev. **168**, 1266 (1968).

[24] Y. Horikawa, Y. Torizuka, A. Nakada, S. Mitsunobu, Y. Kojima, and M. Kimura, Phys. Lett. **36B**, 9 (1971).

[25] H. Zarek, S. Yen, B. O. Pich, T. E. Drake, C. F. Williamson, S. Kowalski, C. P. Sargent, W. Chung, B. W. Wildenthal, M. Harvey, and H. C. Lee, Phys. Lett. **80B**, 26 (1978).

[26] M. P. Fewell, S. Hinds, D. C. Kean, and T. H. Zabel, Nucl. Phys. **A319**, 214 (1979).

[27] D. L. Hillis, E. E. Gross, D. C. Hensley, C. R. Bingham, F. T. Baker, and A. Scott, Phys. Rev. C **16**, 1467 (1977).

[28] P. M. Endt and C. van der Leun, Nucl. Phys. **A214**, 1 (1973).

[29] G. S. Blanpied, N. M. Hintz, G. S. Kyle, M. A. Franey, S. J. Seestrom-Morris, R. K. Owen, J. W. Palm, D. Denhard, M. L. Barlett, C. J. Harvey, G. W. Hoffmann, J. A. McGill, R. P. Lijestrand, and L. Ray, Phys. Rev. C **25**, 422 (1982).

[30] H. Rebel, G. W. Schweimer, G. Schatz, J. Specht, R. Lohken, G. Hauser, D. Habs, and H. Klewe-Nebenius, Nucl. Phys. **A182**, 145 (1972).

[31] Y. Abgrall, B. Morand, and E. Caurier, Nucl. Phys. **A192**, 372 (1972).

[32] J. B. McGrory, private communication.

[33] D. Pelte, O. Häusser, T. K. Alexander, and H. C. Evans, Can. J. Phys. **47**, 1929 (1969).

[34] O. Häusser, B. W. Hooten, D. Pelte, T. K. Alexander, and H. C. Evans, Can. J. Phys. **48**, 35 (1970).

[35] D. Vitoux, R. C. Haight, and J. X. Saladin, Phys. Rev. C **3**, 718 (1971).

[36] D. Schwalm, A. Bamberger, P. G. Bizzeti, B. Povh, G. A. P. Engelbertink, J. W. Olness, and E. K. Warburton, Nucl. Phys. **A192**, 449 (1972).

[37] S. F. Biagi, W. R. Phillips, and A. R. Barnett, Nucl. Phys. **242**, 160 (1975).

[38] M. P. Fewell, S. Hinds, D. C. Kean, and T. H. Zabel, Nucl. Phys. **A319**, 214 (1979).

[39] M. R. Gunye, Phys. Lett. **37B**, 125 (1971).